

Structural Study of Polystyrene-*b*-Poly(acrylic acid) Micelles Complexed with Uranyl: A SAXS Core-Shell Model Analysis

Qiang Tian, Di Zhang, Na LI, Mark Julian Henderson, Qintang Li, Guy Royal, Jérémie Courtois, Minhao Yan, Zhichao Zhu, and Laszlo Almasy

Langmuir, **Just Accepted Manuscript** • DOI: 10.1021/acs.langmuir.9b03934 • Publication Date (Web): 10 Apr 2020

Downloaded from pubs.acs.org on April 15, 2020

Just Accepted

“Just Accepted” manuscripts have been peer-reviewed and accepted for publication. They are posted online prior to technical editing, formatting for publication and author proofing. The American Chemical Society provides “Just Accepted” as a service to the research community to expedite the dissemination of scientific material as soon as possible after acceptance. “Just Accepted” manuscripts appear in full in PDF format accompanied by an HTML abstract. “Just Accepted” manuscripts have been fully peer reviewed, but should not be considered the official version of record. They are citable by the Digital Object Identifier (DOI®). “Just Accepted” is an optional service offered to authors. Therefore, the “Just Accepted” Web site may not include all articles that will be published in the journal. After a manuscript is technically edited and formatted, it will be removed from the “Just Accepted” Web site and published as an ASAP article. Note that technical editing may introduce minor changes to the manuscript text and/or graphics which could affect content, and all legal disclaimers and ethical guidelines that apply to the journal pertain. ACS cannot be held responsible for errors or consequences arising from the use of information contained in these “Just Accepted” manuscripts.

1
2
3
4
5
6
7
8
9
10
11
12
13
14
15
16
17
18
19
20
21
22
23
24
25

Structural Study of Polystyrene-*b*-Poly(acrylic acid) Micelles Complexed with Uranyl: A SAXS Core- Shell Model Analysis

26
27
28
29
30
31
32
33
34
35
36
37
38
39
40
41
42
43
44
45

Qiang Tian^{1*}, *Di Zhang*¹, *Na Li*², *Mark Julian Henderson*¹, *Qintang Li*¹, *Guy Royal*^{1,3}, *J r mie Courtois*¹, *Minhao Yan*^{1*}, *Zhichao Zhu*⁴, *L szl  Alm sy*^{1,5}

46
47
48
49
50
51
52
53
54
55
56
57
58
59
60

¹State Key Laboratory of Environment-Friendly Energy Materials, School of Materials Science and Technology, Southwest University of Science and Technology, Mianyang 621010, China

²National Facility for Protein Science in Shanghai, Zhangjiang Laboratory, No. 233, Haik Road, Shanghai 201204, China

³Univ. Grenoble Alpes, CNRS, DCM, 38000 Grenoble, France

⁴Key Laboratory of Neutron Physics and Institute of Nuclear Physics and Chemistry, China Academy of Engineering Physics, Mianyang 621999, China

⁵Institute for Energy Security and Environmental Safety, Centre for Energy Research, P.O. Box 49, H-1525 Budapest, Hungary

*Corresponding author

Email: tqsuperego@163.com (Q. Tian); yanminhao@swust.edu.cn (M. Yan)

Abstract

The interactions between natural colloidal organic matter and actinides in solutions are complex and not fully understood. In this work, a crew-cut PS-*b*-PAA micelle is proposed as a model particle for humic acid (HA) colloid with the aim to better understand the sequestration, aggregation, and mobility of HA colloids in the presence of uranyl ions. The effects of uranyl ions on the structure of polystyrene-*b*-poly(acrylic acid) (PS_{29k}-*b*-PAA_{5k}) micelles in aqueous solution were mainly investigated by synchrotron small-angle X-ray scattering. A core-shell model, accounting for the thickness and contrast changes of the PAA corona induced by the adsorption of uranyl, was employed to analyze the scattering data. A combination of transmission electron microscopy, dynamic light scattering and zetametry showed a strong affinity of uranyl ions for PAA segments in water at pH 4-5 that resulted in the shrinkage and improved contrast of the PAA corona, as well as colloidal destabilization at high uranyl concentration.

Keywords: polystyrene-*b*-poly(acrylic acid), micelles, uranyl, SAXS, core-shell, adsorption

INTRODUCTION

Uranium is an essential element for nuclear energetic and military applications. In aqueous media such as natural water and wet soil in acidic to near-neutral pH conditions uranium mainly exists as linear and symmetric UO₂²⁺ (uranyl) ion, and its oxides and hydroxides [1, 2], including cationic clusters, show extensive complexation reactions with inorganic and organic-contaminants. The behavior and fate of uranium species in ecosystem is an important issue because

1
2
3 of their toxic and radioactive hazards, and also for the extraction and potential reprocessing of
4
5 nuclear fuel.
6

7
8 The interactions between UO_2^{2+} or its complexes and natural matter include several types of
9
10 chemical and physical processes: absorption/ion-exchange, adsorption/surface sorption, surface
11
12 precipitation, complexation, or formation of colloids [3-5]. In particular, the absorption/ion-
13
14 exchange between uranyl cations and the compensation ions in clay interlayers has been
15
16 extensively investigated [2, 6-9]. A recent grazing-incidence X-ray scattering study of
17
18 vanadium(IV) hydroxide/clay-colloid films, in which V(IV) was used as a substitute for Pu(IV),
19
20 supports the view that stable mineral colloids could affect the transport of actinide contaminants
21
22 [10]. In a natural environment, the situation is further complicated due to the presence of other co-
23
24 contaminants including natural organic matter (NOM) in colloidal form.
25
26

27
28 In view of the nanometer size and unique chemical activity, the interactions between uranyl ions
29
30 and colloidal NOM is likely to play a key role in the mobility, distribution, transport and
31
32 sequestration processes of uranium [11-14]. Lin *et al.* [11] evaluated the tendency of various
33
34 radionuclides to partition into colloidal or truly dissolved fractions. They found that humic acid
35
36 (HA) substances could retard the movement of anthropogenic ^{237}Np in field polluted environments.
37
38 Bednar *et al.* [12] showed that HA generally decreased uranium sorption to minerals because
39
40 uranium has higher affinity to the organic phase. Jackson *et al.* [13] suggested that the uranium is
41
42 predominantly either complexed by dissolved humic substances or bound to its colloids. Despite
43
44 these studies, understanding of the mechanisms of interactions between uranyl ions and colloidal
45
46 NOM is still limited, especially at nano- and molecular scales.
47
48
49

50
51 The size and surface charge of HA colloids depend on sample origin, molecular weight
52
53 distribution, pH and ionic strength of the dispersion, as well as the metal loading. Humic
54
55
56
57
58
59
60

1
2
3 substances contain complex mixtures of polymorphs which are difficult to fully characterize.
4
5 Because of this complexity, these objects have not yet been standardized or mimicked by
6
7 representative systems which could be adopted by researchers[15]. Considering these remarks, we
8
9 propose here core-shell polystyrene-*b*-poly(acrylic acid) (PS-*b*-PAA) micelles as a model system
10
11 for HA colloidal particles. The structure of HA has often been described by a number of small
12
13 aromatic organic acids (e.g., benzoic acid, salicylic, and phthalic) [16] in which carboxylic acid is
14
15 the main functional group. Poly(acrylic acid) is a common model for studying the complex
16
17 formation of polyelectrolytes with metal ions [17-19]. Indeed, HA has intrinsic surfactant-like
18
19 tendencies [20] and by using the small-angle X-ray scattering (SAXS) methods, Kawahigashi *et*
20
21 *al.* [21] proposed that HA colloids in solution are composed of a star-shaped structures with a
22
23 spherical core and flexible branches. Thus, self-organized PS-*b*-PAA micelles in solutions can be,
24
25 to some extent, analogous to HA colloids. Specifically, PS core acts as high density colloidal core,
26
27 and PAA corona behaves as the flexible functional groups, where O-donors in carboxylic acid are
28
29 the main binding groups.
30
31
32
33
34

35 The first objective of this work is to establish a PS-*b*-PAA micelle model as a surrogate for
36
37 studying the interactions of HA colloid and heavy metals. The second objective is to study the
38
39 effects of uranyl ions on the structure of PS-*b*-PAA micelles in weak acid aqueous solutions. We
40
41 use synchrotron SAXS method and show for the first time its power and sensitivity to the studied
42
43 system. The core-shell model, applied to the diblock copolymer micelle, accounts for the
44
45 morphology and contrast changes induced by the adsorption of uranyl, giving physically realistic
46
47 fits to the scattering data. The results show that the uranyl has a strong affinity for the PAA
48
49 segments, resulting in the shrinkage and improved contrast of the PAA corona after adsorption of
50
51 uranyl.
52
53
54
55
56
57
58
59
60

EXPERIMENTAL

PS-*b*-PAA diblock copolymer with number-average molecular weight (M_N) of 27 – 31 k and 4 – 6 k for PS and PAA respectively, was purchased from Sigma-Aldrich Co. 150 mg of PS-*b*-PAA were dissolved into 5 mL N,N-dimethylformamide (DMF), and subsequently, 8 mL of water were added dropwise to the previous solution under stirring in order to induce aggregation of the polystyrene core. The dispersion was then dialyzed into 1000 mL of deionized water during two days to remove the excess DMF. The concentration of the prepared PS-*b*-PAA aqueous dispersion was 10 mg/mL. For comparison, 10 mg/mL PS-*b*-PAA dispersions in mixed DMF/H₂O solutions with H₂O content of 50% and 80% were prepared. Uranyl nitrate hexahydrate [UO₂(NO₃)₂·6H₂O] was obtained from Hubei Chushengwei Chemical Co., Ltd (China). UO₂(NO₃)₂ solutions (0.1 mL) with different concentrations (1, 3, 5, 7, and 10 mg/mL) were slowly added into the PS-*b*-PAA dispersions (0.9 mL, 10 mg/mL) under stirring: these samples were referred as PS-*b*-PAA-*n*UO₂ (with *n* = 1, 3, 5, 7, and 10, respectively).

The SAXS measurements were conducted at the BL19U2 station of the National Center for Protein Science Shanghai in Shanghai Synchrotron Radiation Facility [22]. The scattering intensity $I(q)$ was measured as a function of scattering vector magnitude $q = 4\pi\sin\theta/\lambda$, where $\lambda = 0.103$ nm is the wavelength of the incident X-rays, and θ is half of the scattering angle. A Pilatus 1 M detector (DECTRIS Ltd) with pixel size of 172 μm was employed to record the scattering intensity. The detector was placed at 2667 mm from the sample, resulting in a q range of 0.07 to 3.6 nm^{-1} . A flow cell made of quartz capillary with a diameter of 1.5 mm and a wall-thickness of 10 μm was used to withdraw an aliquot of dispersion. Data were normalized to the intensity of the transmitted X-

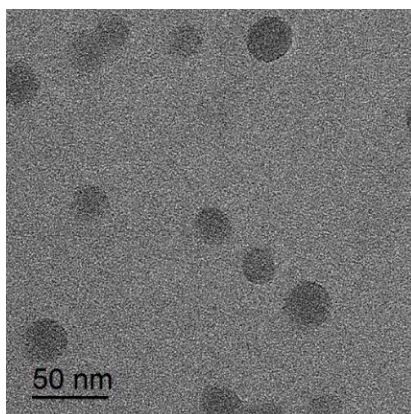
1
2
3 ray beam and corrected for background scattering using the software BioXTAS RAW [23]. Fitting
4
5 of the experimental data to analytical model functions was performed by the method of least
6
7 squares using the SASfit software (version 0.94.6) [24].
8
9

10 The dynamic light scattering (DLS) and zeta potential data were recorded using a NanoBrook
11
12 Omni (Brookhaven, USA) instrument. Transmission electron microscopy (TEM) was carried out
13
14 on a Zeiss Libra 200FE microscope. The uranyl concentration in dispersion was measured by
15
16 inductively coupled plasma optical emission spectrometry (Agilent 730, Agilent Technologies,
17
18 USA).
19
20

21 **CORE-SHELL MODEL**

22
23
24

25 The TEM measurements show that the PS-*b*-PAA copolymer in water produced spherical
26
27 micelles with narrow size distribution (Figure 1). They consist of a PS core (20 ~ 25 nm in
28
29 diameter) with the surface covered by the PAA chains forming the corona. This is the most
30
31 common morphology reported for block copolymer micelles [25, 26]. Since the contrast in the
32
33 electron density between the copolymer blocks is low, it was not possible to distinguish the corona
34
35 layer from the PS core by TEM.
36
37



51
52 **Figure 1.** TEM micrograph of the PS-*b*-PAA micelles.
53
54
55
56
57
58
59
60

To extract more information, the scattering data were analyzed by fitting model functions to the $I(q)$ curves. Prior to fitting, the scattering length density (SLD) distribution of a micelle along the radial direction was estimated. Generally, the PS core is believed to have a homogeneous structure which can be described by a solid sphere model. In contrast, the SLD distribution in the PAA corona is more complicated because many factors such as the ionization degree, ionic strength, repulsion among PAA chains, as well as PAA density and molecular weight influence the spatial distribution of the chains. [27]. The star model considers that the density of the corona decreases with increasing distance from the core [28], while the mean-field model assumes that the corona shell has a uniform concentration of polymer segments [29, 30]. As pointed out by de Gennes, the mean-field model is best suited for micelles with thin and continuous coronas [30], the so-called crew-cut micelles [26]. In this work the sample has a degree of polymerization of the PS block of 279 and the PAA block of 69, *i.e.*, the PAA corona thickness is much smaller than the radius of the PS core. Therefore, the PS(279)-*b*-PAA(69) micelles are assumed to have a uniform shell consisting of PAA and solvent.

From a mathematical consideration, in the case of a spherical particle with a uniform scattering length density (ρ) embedded in a homogeneous medium (liquid or solid), the radiation scattering amplitude is written as:

$$F(q)_{\text{sphere}} = 4\pi\Delta\rho_{\text{sphere}} \int_0^{R_1} \frac{\sin qr}{qr} r^2 dr = \Delta\rho_{\text{sphere}} V_{\text{sphere}} j(qR) \quad (1)$$

where $\Delta\rho_{\text{sphere}} = \rho_m - \rho$, ρ_m is the scattering length density of the medium, R is the radius of sphere, and $j(x) = 3(\sin x - x \cos x)/x^3$. The scattering amplitude of a core-shell structure with uniform inner core and outer shell can be deduced from eq. 1,

$$F(q)_{\text{core-shell}} = \Delta\rho_{\text{shell}} V_{\text{core-shell}} j(qR_{\text{core}} + q\Delta R) - (\Delta\rho_{\text{shell}} - \Delta\rho_{\text{core}}) V_{\text{core}} j(qR_{\text{core}}) \quad (2)$$

where R_{core} and ΔR are the inner radius and shell thickness, $\Delta\rho_{\text{shell}}$ and $\Delta\rho_{\text{core}}$ are the excess SLD of the core and the shell to the surrounding medium, respectively. Herein, the non-uniformity in size of the PS cores is accounted by their size distribution, while the shell thickness is assumed to be uniform. For a dilute polydisperse core-shell particle system, the scattering intensity in absolute scale is written as:

$$I(q) = \int_0^{\infty} N(R_{\text{core}}) F^2(q, R_{\text{core}}, \Delta R) dR_{\text{core}} \quad (3)$$

where $N(R_{\text{core}})$ is the size distribution of the inner core, which can be conveniently described by a normal distribution,

$$N(R_{\text{core}}) = \frac{N_0}{\sigma\sqrt{2\pi}} \exp\left(-\frac{(R_{\text{core}} - R_0)^2}{2\sigma^2}\right) \quad (4)$$

where R_0 is the mean radius, σ the standard deviation, and N_0 the number density (the total number of particles per unit volume). The scattering curve shape of a core-shell particle is determined by the core radius and shell thickness, and by their contrasts $\Delta\rho_{\text{core}}$ and $\Delta\rho_{\text{shell}}$ with the surrounding aqueous medium. From visual inspection of the scattering curves, the first oscillation peak in the scattering curve of a core-shell particle is often sharp and broad as compared with that of a solid spherical particle with similar overall size [31].

Table 1. Calculated X-ray scattering length densities.

	density (g/cm ³)	ρ_e (cm ⁻²)	normalized ρ_e
H ₂ O	1.00	9.42×10^{10}	1
PS	1.04	9.50×10^{10}	1.01
PAA	1.20	1.07×10^{11}	1.14

The actual X-ray SLD of the PS core can be assumed to be similar to the calculated value in Table 1, given the hydrophobic nature of PS and the nearly similar SLD of water and PS. However,

1
2
3 the water content in the PAA shell is not known. The corona PAA chains have a substantially
4 higher SLD than both the solvent and the PS core, making the micelle essentially similar to a shell
5 particle. After sorption of the UO_2^{2+} ions, the PAA shell's SLD further increases due to very high
6 X-ray scattering length of the uranium atom. This information will be used as the prior information
7 before model fitting.
8
9
10
11
12
13

14 RESULTS AND DISCUSSION

15
16
17
18 **PS-*b*-PAA Micelles.** The SAXS curves obtained from the PS-*b*-PAA micelles in H_2O and
19 DMF/ H_2O solutions are shown in Figure 2. With increasing H_2O ratio in H_2O /DMF solutions the
20 oscillation peaks shift toward high q indicating the decrease in the micelle size (Figure 2a), which
21 is induced by the removal of DMF from the PS cores. The development of the broad first oscillation
22 peak indicates the formation of core-shell PS-*b*-PAA micelles. Neither the solid sphere nor the
23 spherical shell gave a satisfactory fit to the experimental data, as shown by the dash and dash dot
24 lines in Figure 2b. In addition, an attempt to fit the shell with exponential contrast profile also
25 failed. In agreement with our work, Wang *et al.* [27] have demonstrated that the uniform shell
26 model described well the SAXS data obtained from PAA brushes grafted on PS particle core. The
27 core-shell model fitted results are shown in Table 2. Note that the core-shell model works at $\Delta R =$
28 0 for the micelles in the mixed solution with 50% H_2O , i.e., the micelles appear as spherical
29 particles.
30
31
32
33
34
35
36
37
38
39
40
41
42
43
44
45
46
47
48
49
50
51
52
53
54
55
56
57
58
59
60

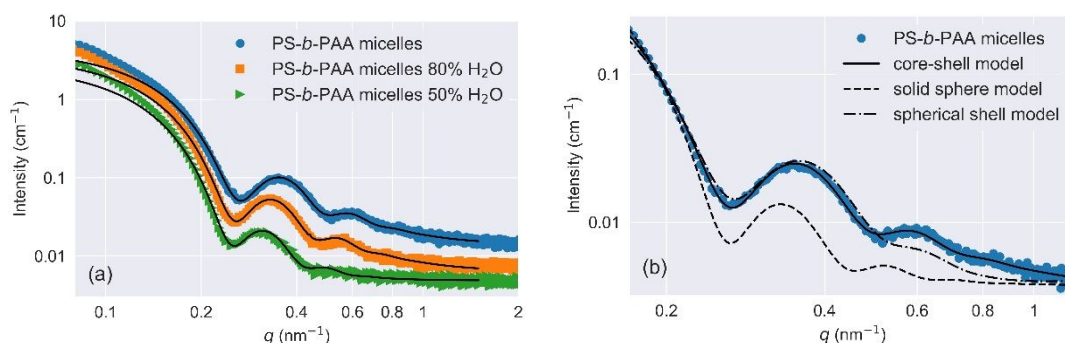


Figure 2. SAXS curves obtained from PS-*b*-PAA micelles in H₂O and DMF/H₂O solutions; the curves are shifted vertically by factors of 2 and 4 for clarity; black lines are the fits to core-shell model (a). Model fitting to the SAXS data of PS-*b*-PAA micelles in H₂O; the solid, dash, and dash dot lines denote the fits to core-shell, solid sphere, and spherical shell models, respectively (b).

The core-shell model fit to the data of PS-*b*-PAA micelles in H₂O yields an average radius (R_0) of 11.1 nm with a standard deviation of 1.6 nm (Table 2). Accordingly, the average aggregation number (N_{agg}) of a micelle can be estimated by $4\pi R_0^3/3V_{\text{PS}}$, where V_{PS} is the volume of a PS(279) block in a PS-*b*-PAA molecule; the surface area per corona chain (A_c) is calculated as $4\pi R_0^2/N_{\text{agg}}$. In average, there are 135 PAA(69) chains that emanate from the PS core, and each PAA chain occupies 12 nm² surface area of the PS core. In addition, the core-shell model could satisfactorily describe the featured oscillation peaks, while the calculated intensities are smaller than experimental intensities at the low q region. This results indicate that some PS-*b*-PAA copolymer assembled into bigger particles. During TEM observations, we found a very small proportion of particles with size around 50 nm. The results are also in agreement with the measured hydrodynamic diameter ($D_H = 145$ nm) of PS-*b*-PAA in H₂O (Table 3).

Table 2. Structural parameters obtained from SAXS data on PS-*b*-PAA micelles by curve fitting using a core-shell model.

H ₂ O	DMF	R_0 (nm)	σ (nm)	ΔR (nm)	N_{agg}	S_{core} (nm ²)	A_c (nm ²)
100%	0	11.1(1)	1.6(1)	2.6(2)	135	1641	12
80%	20%	12.6(2)	1.7(1)	2.4(2)	-	-	-
50%	50%	17.6(1)	1.7(1)	0 (fixed)	-	-	-

PAA is a water-soluble weak polyelectrolyte with a pK_a value between 4.5 and 5 [32, 33]. The pH value of the as-prepared PS-*b*-PAA dispersion is 4.5 implying that the degree of ionization of

1
2
3 PAA is about 50%. The ionization degree strongly affects the chain conformation of
4 polyelectrolyte in aqueous solutions. PAA chains incline to adapt the coiled conformation when
5
6 pH is lower, while the polymer chains become more stretched due to the repulsion among the
7
8 ionized carboxylic groups when the pH value is higher, [34, 35]. Assuming that the PAA corona
9
10 chains adopt a self-avoiding walk model in a good solvent, the gyration radius (R_g) can be
11
12 calculated as $R_g = aN^{0.6}/6^{0.5}$, where a is the step length (monomer size), which is taken as 0.25 nm
13
14 for PAA, and N is the number of steps (degree of polymerization) [17, 36]. The estimated $2R_g$ is
15
16 2.56 nm, in accordance with the fitted corona thickness (ΔR). The calculated projection area of a
17
18 PAA chain on the PS core is about 7.9 nm², which is smaller than A_c (12 nm²). In order to decrease
19
20 the interfacial energy between the PS core and the solvent, the PAA chains extend in the lateral
21
22 direction to cover the PS surface, which is balanced by the repulsion among the corona chains.
23
24
25
26
27

28 The micelle morphology can be influenced by the asymmetry of PS-*b*-PAA diblock. On the one
29
30 hand, if the PAA length is too short, the micelles can adopt rod-like, vesicular and highly
31
32 polydisperse morphologies [26]. On the other hand, if the PAA length is too long, the micelles will
33
34 form a spherical polyelectrolyte brush, which is uncharacteristic for HA colloids. Hence, in this
35
36 work, a moderate asymmetric PS(279)-*b*-PAA(69) diblock, which forms crew-cut micelles in
37
38 aqueous solution with spherical PS core and uncrowded PAA coronas, was employed to simulate
39
40 the HA colloids.
41
42
43

44 **PS-*b*-PAA Micelles with Uranyl Ions.** The scattering and fitted curves of PS-*b*-PAA micelles
45
46 mixed with uranyl nitrate are shown in Figure 3a. With increasing UO_2^{2+} concentration, slight
47
48 changes can be observed in the shape of the first oscillation peaks, and the second oscillation peaks
49
50 become stronger. A zoom-in of the data for the q range of 0.2 to 0.8 nm⁻¹ is shown in Figure 3b.
51
52 As the UO_2^{2+} concentration was increased from 0 to 0.2 mM as well as from 0.6 to 1 mM, only the
53
54
55
56
57
58
59
60

maximum intensities of the oscillation peaks increase, while the troughs of the oscillation peaks remain unchanged. Since the overall intensity has a monotonous change with the PAA corona thickness or contrast, this behavior should be induced by the inverse change of ΔR and $\Delta\rho_{\text{shell}}$. During fitting, the parameters of σ , ΔR , and $\Delta\rho_{\text{core}}$ are fixed to the values in Table 2. With increasing UO_2^{2+} concentration from 0 to 1 mM, ΔR decreases from 2.58 to 1.85 nm, and $\Delta\rho_{\text{shell}}$ increases from 1.53 to 2.02 in arbitrary units (Figure 4).

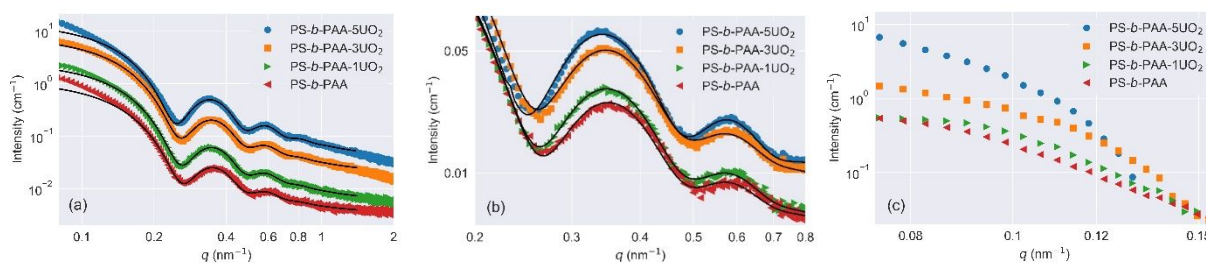


Figure 3. SAXS curves obtained from the PS-*b*-PAA micelles and uranyl nitrate mixtures; the curves are shifted vertically by factors of 2, 4, and 8 for clarity; black lines are the best fits to core-shell model (a). A zoom-in of (a) in the medium q range (b). Deviation between the experimental and fitted data at the low q region (c). PS-*b*-PAA-7UO₂/10UO₂ samples were not evaluated because they showed precipitations.

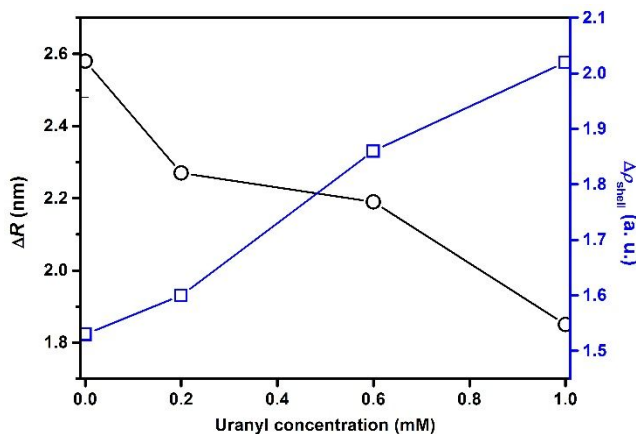


Figure 4. PAA corona thickness ΔR and contrast $\Delta\rho_{\text{shell}}$ as a function of uranyl concentration.

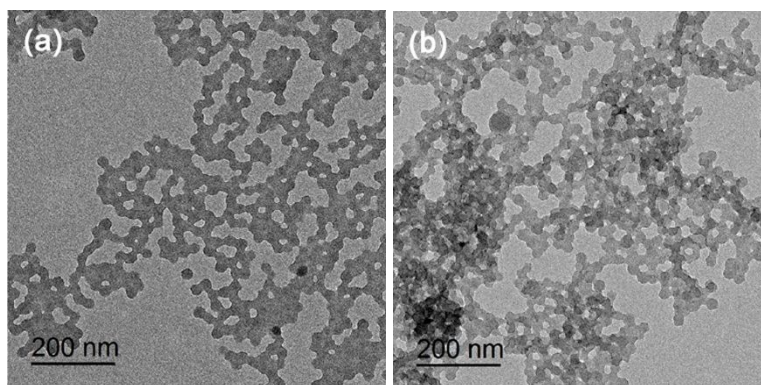


Figure 5. TEM micrographs of the PS-*b*-PAA-1UO₂ (a) and PS-*b*-PAA-5UO₂ (b).

Table 3. Dynamic light scattering and zeta potential data of PS-*b*-PAA-*n*UO₂ dispersions.

samples	UO ₂ ²⁺ (mM)	<i>D</i> _H (nm)	ζ (mV)	pH
PS- <i>b</i> -PAA	0	145(3)	-26(2)	4.5
PS- <i>b</i> -PAA- 1UO ₂	0.2	138(2)	-4(1)	5.1
PS- <i>b</i> -PAA- 3UO ₂	0.6	155(1)	-9(2)	4.2
PS- <i>b</i> -PAA- 5UO ₂	1	265(5)	-16(1)	4.1
PS- <i>b</i> -PAA- 7UO ₂	1.4	960(23)	Partial precipitation	

The deviations between the experimental and fitted data are shown in Figure 3c. Compared with the other samples, PS-*b*-PAA-5UO₂ exhibits obvious up-turn in the curves, an indication of an attractive interaction between the PS-*b*-PAA micelles induced by uranyl. However, the morphology of these intermicellar aggregates cannot be determined due to the low *q* limit. The TEM observation also shows the significant aggregation of the PS-*b*-PAA micelles at high UO₂²⁺ concentration (Figure 5). In contrast, no intermicellar aggregation is observed by TEM for pure PS-*b*-PAA micelles (Figure 1). Compared to the pH of pure uranyl solution (0.2 mM, pH = 4.7), the increase of pH to 5.1 for the PS-*b*-PAA-1UO₂ sample (Table 3) is probably due to the reversible hydrolysis reactions of uranyl (at the pH range of 4 to 5, UO₂²⁺ is around 69%, UO₂OH⁺ is less

1
2
3 than 26%, and $(\text{UO}_2)_2(\text{OH})_2^{2+}$ is less than 5% [37]). This result implies that the uranyl
4 concentration was lowered by the adsorption by PAA segments, leading to the increase of the
5 solution pH. Note that higher pH (>5) induces the precipitate of uranyl in solution, while lower pH
6 (<4) leads to the destabilization of the PS-*b*-PAA micelles because of their low degree of
7 ionization. In this work, the pH did not rise beyond 5.1, therefore the complexation between uranyl
8 and PAA rather than bulk precipitation of uranyl hydroxide/oxide most likely occurred.
9

10
11
12
13
14
15
16
17 The absolute zeta potential (ζ) of PS-*b*-PAA micelles with uranyl is smaller than that of PS-*b*-
18 PAA and the D_H of PS-*b*-PAA-5 UO_2 /7 UO_2 is significantly larger than that of PS-*b*-PAA (Table
19 3). A series of PS-*b*-PAA micelle samples with different pH were prepared for comparison. The ζ
20 of these control samples increased from -42 to -20 mV as the pH decreased from 6.2 to 3.3. The
21 D_H for the reference PS-*b*-PAA micelles at pH 4.1 was 139 nm, an indication that the pH did not
22 have a significant influence on ζ and D_H compared with the complexation of the micelles by uranyl.
23 Hence, these results suggest that the negative charges of PAA corona are compensated by the
24 positively charge uranyl solution species, e.g., UO_2^{2+} and UO_2OH^+ leading to the aggregation of
25 the PS-*b*-PAA micelles. Small-angle scattering, DLS, zetametry, and TEM all prove that the PAA
26 corona chains have strong interactions with the UO_2^{2+} cations.
27
28
29
30
31
32

33
34
35
36
37
38
39
40 Swiech *et al.* [20] and Shang *et al.* [38] reported a featured R_g value of ~ 10 nm for HA colloids,
41 which may correspond to the primary particle size of HA colloids in their samples. Angelico *et al.*
42 [39] reported that the ζ of HA-Fe colloids ranged from -16 to -36 mV at different pH values, and
43 the TEM observation revealed that sponge-like aggregation of HA-Fe was composed of ~ 20 nm
44 spherical particles. The reported size and ζ of HA colloids are comparable to those of the studied
45 PS-*b*-PAA micelles. Therefore, from size and charge point of view, it is reasonable to consider the
46 PS(279)-*b*-PAA(69) micelles as representative of the colloidal behavior of HA.
47
48
49
50
51
52
53
54
55
56
57
58
59
60

1
2
3 Further increase in the concentration of UO_2^{2+} ions ($> 1 \text{ mM}$) leads to the precipitation of the
4 PS-*b*-PAA micelles, *e.g.*, the PS-*b*-PAA-10U sample exhibits a complete precipitation. An aliquot
5 of the supernate was measured by ICP-OES to estimate the adsorption performance of PS-*b*-PAA
6 micelles as calculated from the uranyl concentration variation and SAXS results. On average, 1
7 PS(279)-*b*-PAA(69) micelle can adsorb ~ 600 uranyl species, *i.e.*, 15 acrylic acid segments can
8 accommodate 1 uranyl.
9

10
11 It has been reported that the complexing ability of uranyl cations with PAA molecules is the
12 highest among the common heavy metal ions (in the order: $\text{UO}_2^{2+} > \text{Cu}^{2+} > \text{VO}^{2+} > \text{Co}^{2+} > \text{Ni}^{2+} >$
13 Zn^{2+}) [18, 40], with a 2:1 stoichiometry of the PAA/ UO_2^{2+} complex [41]. This work supports the
14 view that formation of the stable PAA/ UO_2^{2+} complexes is the reason for the observed decrease of
15 the PAA corona thickness, the increase of the corona contrast, as well as the aggregation of the
16 PS-*b*-PAA micelles.
17

18
19 Combining the advantages of quasi-monodisperse crew-cut PS-*b*-PAA micelles and synchrotron
20 SAXS, the structure of PS-*b*-PAA micelles influenced by uranyl cations can be resolved by model
21 fitting. The PS-*b*-PAA micelles exhibit featured scattering with pronounced oscillations, and
22 because of the sensitivity of X-rays to heavy metals, such as uranium, the feasibility of applying
23 SAXS to explore the detailed structural changes in the PAA shell influenced by uranyl is ensured.
24 Furthermore, the data acquisition time for one PS-*b*-PAA micelle sample at SSRF BL19U2 is only
25 1 second, which is enough to give good statistics for data analysis. Hence synchrotron SAXS is an
26 effective tool to study the effects of interactions between PS-*b*-PAA micelles and uranyl ions.
27

28
29 We should stress that the proposed micelle model is still a simple one with respect to the real
30 HA colloids-uranyl interactions. Hence, this study can be used as a guide to physical and chemical
31 insights of the effects of the primary interactions. The traditional studies on the interactions
32
33
34
35
36
37
38
39
40
41
42
43
44
45
46
47
48
49
50
51
52
53
54
55
56
57
58
59
60

1
2
3 between HA colloids and uranyl or other metal cations are complicated by their diversity and
4 incomplete understanding of their natures. More explicit results in colloidal respect are obtained
5 from the PS-*b*-PAA micelle model, which bridge the gap in similar studies. Due to the analogous
6 properties of PS(279)-*b*-PAA(69) and HAs colloids, we infer that the colloidal HA could form
7 stable complexes and change structural configuration with adsorbing uranyl, enable uranyl to
8 transport and affect the fate of uranyl in aquatic ecosystem, as well as aggregate and precipitate at
9 high uranyl concentration. The developed method could be useful for future studies, including the
10 adsorption mechanism of HA, their interactions with other inorganic and organic co-contaminants,
11 environment remediation, as well as tracer particles to detect the transport behavior of actinides
12 under the influence of HA colloids. The limitation of this work is that other functional groups
13 existing in HA and capable of uranyl binding such as catechol, hydroquinone, 2-
14 hydroxyacetophenone and quinone [42] have not been considered. Developing new model
15 micelles with different functional groups for simulating HA colloids deserves thus further studies.
16
17
18
19
20
21
22
23
24
25
26
27
28
29
30
31

32 **CONCLUSIONS**

33
34
35 This study indicated that the crew-cut PS-*b*-PAA micelles can be used to represent the
36 interactions between HA colloids and actinide solution species. By virtue of the monodisperse
37 PS(279)-*b*-PAA(69) micelles and the synchrotron X-ray radiation, the detailed microstructure of
38 the micelles influenced by uranyl ions can be resolved by the core-shell model fitting. With
39 increasing UO_2^{2+} concentration from 0 to 1 mM, the PAA shell thickness decreased from 2.6 to
40 1.9 nm, and the shell contrast increased from 1.5 to 2.0 in arbitrary units. PS(279)-*b*-PAA(69)
41 micelles showed strong affinity to aqueous uranyl ions. One such micelle can adsorb about 600
42 uranyl cations and their hydrolyzed species. Higher UO_2^{2+} concentration (> 1 mM) promoted the
43 aggregation and precipitation of the PS-*b*-PAA micelles. A series of work in terms of nuclear waste
44
45
46
47
48
49
50
51
52
53
54
55
56
57
58
59
60

1
2
3 treatment, environment remediation, and transport of actinides can be done based on the methods
4
5 and results reported in this work.
6
7

8 **AUTHOR INFORMATION**

9

10 **Corresponding Author**

11
12
13 *E-mail: tqsuperego@163.com (Q. Tian); yanminhao@swust.edu.cn (M. Yan)
14
15

16 **Author Contributions**

17
18
19 The manuscript was written through contributions of all authors. All authors have given
20
21 approval to the final version of the manuscript.
22
23

24 **Funding Sources**

25
26
27
28 National Natural Science Foundation of China under grant no. 11775195; the scientific research
29
30 fund of Southwest University of Science and Technology (18zx7108).
31
32

33 **Notes**

34
35
36 The authors declare no competing financial interest.
37
38
39

40 **ACKNOWLEDGMENT**

41
42 This work was supported by the National Natural Science Foundation of China under grant no.
43
44 11775195, the scientific research fund of Southwest University of Science and Technology
45
46 (18zx7108). We thank the staffs from BL19U2 beamline of Nation Facility for Protein Science
47
48 (NFPS) at Shanghai Synchrotron Radiation Facility for assistance during data collection.
49
50

51 **REFERENCES**

- 52
53
54 1. Brookins, D.G. Eh-pH Diagrams For Geochemistry. Springer Science & Business Media, **2012**.
55
56 2. Rosenberg, E.; Pinson, G.; Tsosie, R.; Tutu, H.; Cukrowska, E. Uranium Remediation by Ion
57
58
59

- 1
2
3 Exchange and Sorption Methods: A Critical Review. *Johnson Matthey Tech.* **2016**, *60*, 59–77.
4
5
6 3. Misaelides, P.; Godelitsas, A. Interaction of Actinides with Natural Microporous Materials.
7
8 Natural Microporous Materials in Environmental Technology. Springer: Dordrecht, **1999**.
9
10 4. Tan, X.; Fang, M.; Wang, X. Sorption Speciation of Lanthanides/Actinides on Minerals by
11
12 TRLFS, EXAFS and DFT Studies: A Review. *Molecules* **2010**, *15*, 8431-8468.
13
14
15 5. Geckeis, H.; Lützenkirchen, J.; Polly, R.; Rabung, T.; Schmidt, M. Mineral–Water Interface
16
17 Reactions of Actinides. *Chem. Rev.* **2013**, *113*, 1016–1062.
18
19
20 6. Humelnicu, D.; Popovici, E.; Dvininov, E.; Mita, C. Study on the Retention of Uranyl Ions on
21
22 Modified Clays with Titanium Oxide. *J. Radioanal. Nucl. Chem.* **2009**, *279*, 131–136.
23
24
25 7. Anirudhan, T. S.; Bringle, C. D.; Rijith, S. Removal of Uranium(VI) from Aqueous Solutions
26
27 and Nuclear Industry Effluents Using Humic Acid-Immobilized Zirconium pillared Clay. *J.*
28
29 *Environ. Radioact.* **2010**, *101*, 267–276.
30
31
32 8. Li, S.; Wang, X.; Huang, Z.; Du, L.; Tan, Z.; Fu, Y.; Wang, X. Sorption and Desorption of
33
34 Uranium (VI) on GMZ Bentonite: Effect of pH, Ionic Strength, Foreign Ions and Humic
35
36 Substances. *J. Radioanal. Nucl. Chem.* **2016**, *308*, 877–886.
37
38
39 9. Leng, Y.; Li, Q.; Tian, Q.; Chen, X.; Almásy, L.; Liu, Y.; Sun, G.; Tuo, X.; Yan, M.; Henderson,
40
41 M. J. (Ce-Al)-Oxide Pillared Bentonite: A High Affinity Sorbent for Plutonium. *J. Hazard.*
42
43 *Mater.* **2018**, *352*, 121–129.
44
45
46 10. Song, P.; Li, Q.; Almásy, L.; Tuo, X.; Yan, M.; Henderson, M. J. Fractionation of Clay
47
48 Colloids and Their Synthetic Utility in Vanadium Hydroxide-Clay Thin Film Formation. *Appl.*
49
50 *Surf. Sci.* **2019**, *481*, 92–98.
51
52
53 11. Lin, P.; Xu, C.; Xing, W.; Sun, L.; Kaplan, D. I.; Fujitake, N.; Yeager, C. M.; Schwehr, K. A.;
54
55 Santschi, P. H. Radionuclide Uptake by Colloidal and Particulate Humic Acids Obtained from
56
57
58
59
60

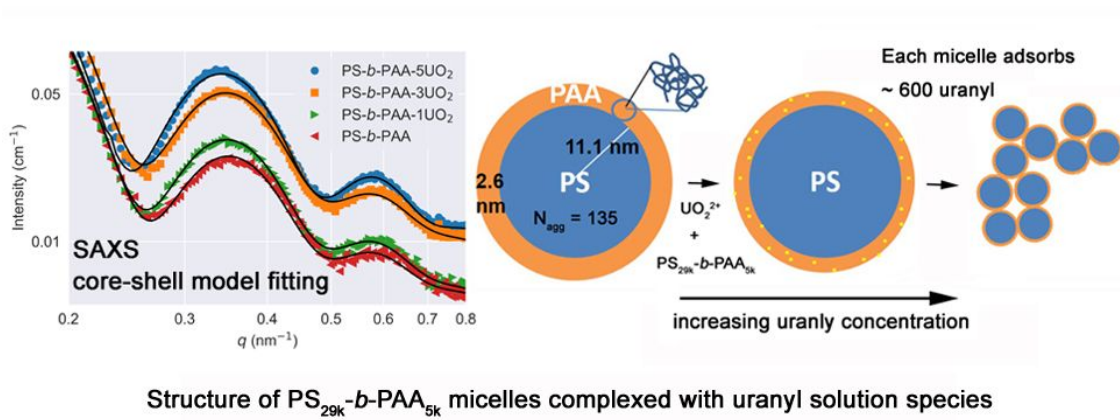
- 1
2
3 14 Soils Collected Worldwide. *Sci. Rep.* **2018**, *8*, 4795.
4
5
6 12. Bednar, A. J.; Medina, V. F.; Ulmer-Scholle, D. S.; Frey, B. A.; Johnson, B. L.; Brostoff, W.
7
8 N.; Larson, S. L. Effects of Organic Matter on the Distribution of Uranium in Soil and Plant
9
10 Matrices. *Chemosphere.* **2007**, *70*, 237–247.
11
12
13 13. Jackson, B. P.; Ranville, J. F.; Bertsch, P. M.; Sowder, A. G. Characterization of Colloidal and
14
15 Humic-Bound Ni And U In the “Dissolved” Fraction of Contaminated Sediment Extracts.
16
17 *Environ. Sci. Technol.* **2005**, *39*, 2478–2485.
18
19
20 14. De Stefano, C.; Gianguzza, A.; Pettignano, A.; Piazzese, D.; Sammartano, S. Uranium (VI)
21
22 Sequestration by Polyacrylic and Fulvic Acids in Aqueous Solution. *J. Radioanal. Nucl. Chem.*
23
24 **2011**, *289*, 689–697.
25
26
27 15. Perminova, I. V.; Frimmel, F. H.; Kudryavtsev, A.V.; Kulikova, N. A.; Abbt-Braun, G.; Hesse,
28
29 S.; Petrosyan, V. S. Molecular Weight Characteristics of Humic Substances from Different
30
31 Environments as Determined by Size Exclusion Chromatography and Their Statistical
32
33 Evaluation. *Environ. Sci. Technol.* **2003**, *37*, 2477–2485.
34
35
36 16. Wood, S. A. The Role of Humic Substances in the Transport and Fixation of Metals of
37
38 Economic Interest (Au, Pt, Pd, U, V). *Ore Geol. Rev.* **1996**, *11*, 1–31.
39
40
41 17. Reith, D.; Müller, B.; Müller-Plathe, F. Wiegand, S. How Does the Chain Extension of Poly
42
43 (Acrylic Acid) Scale in Aqueous Solution? A Combined Study with Light Scattering and
44
45 Computer Simulation. *J. Chem. Phys.* **2002**, *116*, 9100–9106.
46
47
48 18. Roma-Luciow, R.; Sarraf, L.; Morcellet, M. Complexes of Poly (Acrylic Acid) with Some
49
50 Divalent, Trivalent and Tetravalent Metal Ions. *Eur. Polym. J.* **2001**, *37*, 1741–1745.
51
52
53 19. Qi, X.; Wang, Z.; Ma, S.; Wu, L.; Yang, S.; Xu, J. Complexation Behavior of Poly (Acrylic
54
55 Acid) and Lanthanide Ions. *Polymer* **2014**, *55*, 1183–1189.
56
57
58
59
60

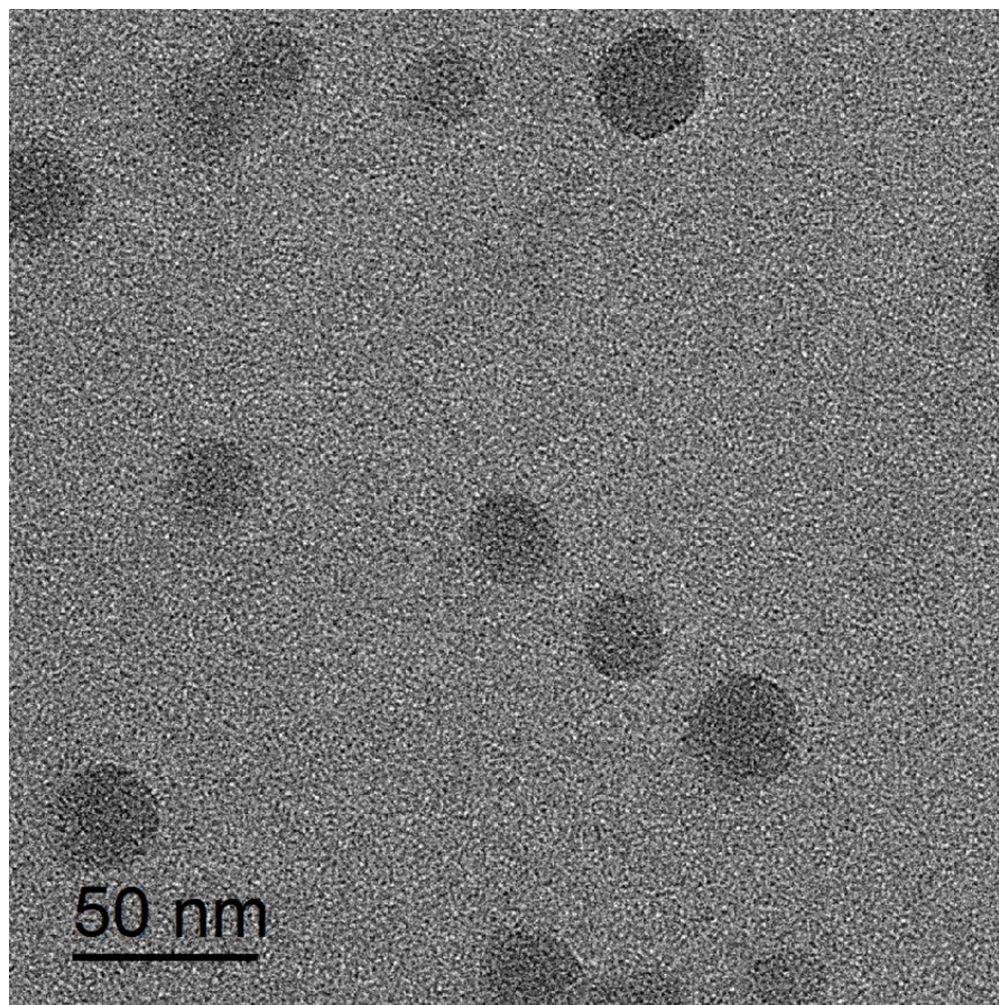
- 1
2
3 20. Swiech, W. M.; Hamerton, I.; Zeng, H.; Watson, D. J.; Mason, E.; Taylor, S. E. Water-Based
4 Fractionation of A Commercial Humic Acid. Solid-State and Colloidal Characterization of the
5 Solubility Fractions. *J. Colloid Interface Sci.* **2017**, *508*, 28–38.
6
7
8
9
10 21. Kawahigashi, M.; Fujitake, N.; Azuma, J.; Takahashi, T.; Kajiwara, K.; Urakawa, H. The
11 Shape of Humic Acid in Solution as Observed by Small-Angle X-Ray Scattering. *Soil Sci.*
12 *Plant Nutr.* **1995**, *41*, 363–366.
13
14
15
16
17 22. Li, N.; Li, X.; Wang, Y.; Liu, G.; Zhou, P.; Wu, H.; Hong, C.; Bian, F.; Zhang, R. The New
18 NCPSS BL19U2 Beamline at the SSRF for Small-Angle X-Ray Scattering from Biological
19 Macromolecules in Solution. *J. Appl. Crystallogr.* **2016**, *49*, 1428–1432.
20
21
22
23
24 23. Hopkins, J. B.; Gillilan R. E.; Skou S. BioXTAS RAW: Improvements to A Free Open-Source
25 Program for Small-Angle X-Ray Scattering Data Reduction and Analysis. *J. Appl. Crystallogr.*
26 **2017**, *50*, 1545–1553.
27
28
29
30
31 24. Breßler, I.; Kohlbrecher, J.; Thünemann, A. F. SASfit: A Tool for Small-Angle Scattering Data
32 Analysis Using A Library of Analytical Expressions. *J. Appl. Crystallogr.* **2015**, *48*, 1587–
33 1598.
34
35
36
37
38 25. Zhang, L. Crew-Cut Aggregates of Polystyrene-B-Poly(Acrylic Acid) Diblock Copolymers in
39 Solutions. McGill University Libraries, **1996**.
40
41
42 26. Zhang L, Eisenberg A. Multiple Morphologies of "Crew-Cut" Aggregates of Polystyrene-B-
43 Poly (Acrylic Acid) Block Copolymers. *Science* **1995**, *268*, 1728–1731.
44
45
46
47 27. Wang, W.; Chu, F.; Li, L.; Han, H.; Tian, Y.; Wang, Y.; Yuan, Z.; Zhou, Z.; Guo, X.
48 Interactions Among Spherical Poly (Acrylic Acid) Brushes: Observation by Rheology and
49 Small Angle X-Ray Scattering. *J. Polym. Sci. B Polym. Phys.* **2016**, *54*, 405–413.
50
51
52
53
54 28. Halperin, A. Polymeric Micelles: A Star Model. *Macromolecules* **1987**, *20*, 2943–2946.
55
56
57
58
59
60

- 1
2
3 29. Noolandi, J.; Hong, K. M. Theory of Block Copolymer Micelles in Solution. *Macromolecules*
4 **1983**, *16*, 1443–1448.
5
6
7
8 30. de Gennes; P. G. In *Solid State Physics, Supplement 14*, Liebert, L. (Ed) Academic Press: New
9 York, **1978**.
10
11
12 31. Zhang, J.; Tian, Q.; Li, Q.; Henderson, M. J.; Tuo, X.; Yan, M.; Almásy, L. Small-angle
13 scattering model analysis of cage-like uranyl peroxide nanoparticles. *J. Mol. Liq.* **2019**, *296*,
14 111794.
15
16
17
18
19 32. Bukhari, S. M. H.; Khan, S.; Rehanullah, M.; Ranjha, N. M. Synthesis and Characterization of
20 Chemically Cross-Linked Acrylic Acid/Gelatin Hydrogels: Effect of pH and Composition on
21 Swelling and Drug Release. *Int. J. Polym. Sci.* **2015**, 187961.
22
23
24
25
26 33. Das, K. K.; Somasundaran, P. Ultra-Low Dosage Flocculation of Alumina Using Polyacrylic
27 Acid. *Colloids Surf. A Physicochem. Eng. Asp.* **2001**, *182*, 25–33.
28
29
30
31 34. Liu, L.; Luo, S. Z.; Wang, B.; Guo, Z. H. Investigation of Small Molecular Weight
32 Poly(Acrylic Acid) Adsorption on γ -Alumina. *Appl. Surf. Sci.* **2015**, *345*, 116–121.
33
34
35 35. Wang, J.; Somasundaran, P. Reversible Conformational Behavior of Poly(Acrylic Acid) LB
36 Film With Changes in pH, Ionic Strength and Time. *Colloids Surf. A Physicochem. Eng. Asp.*
37 **2006**, *273*, 63–69.
38
39
40
41
42 36. Das, K. K.; Somasundaran, P. A. Kinetic Investigation of the Flocculation of Alumina with
43 Polyacrylic Acid. *J. Colloid Interface Sci.* **2004**, *271*, 102–109.
44
45
46
47 37. Zhang, H.; Tao, Z. Sorption of Uranyl Ions on Silica: Effects of Contact Time, pH, Ionic
48 Strength, Concentration and Phosphate. *J. Radioanal. Nucl. Chem.* **2002**, *254*, 103–107.
49
50
51 38. Shang, C; Rice, J. A. Investigation of Humate-Cetyltrimethylammonium Complexes by Small-
52 Angle X-Ray Scattering. *J. Colloid Interface Sci.* **2007**, *305*, 57–61.
53
54
55
56
57
58
59
60

- 1
2
3 39. Angelico, R.; Ceglie, A.; He, J.; Liu, Y.; Palumbo, G.; Colombo, C. Particle Size, Charge and
4 Colloidal Stability of Humic Acids Coprecipitated with Ferrihydrite. *Chemosphere* **2014**, *99*,
5 239–247.
6
7
8
9
10 40. Nishide, H.; Oki, N.; Tsuchida, E. Complexation of Poly(Acrylic Acid)s with Uranyl Ion. *Eur.*
11 *Polym. J.* **1982**, *18*, 799–802.
12
13
14 41. Dubolazov, A. V.; Güven, O.; Pekel, N.; Azhgozhinova, G. S.; Mun, G. A.; Nurkeeva, Z. S.
15 Electrochemical, Spectroscopic, and Thermal Studies on Interactions of Linear Poly(Acrylic
16 Acid) with Uranyl Ions in Aqueous Solutions. *J. Polym. Sci. B Polym. Phys.* **2004**, *42*, 1610–
17 1618.
18
19
20
21
22
23 42. Sundararajan, M.; Rajaraman, G.; Ghosh, S. K. Speciation of Uranyl Ions in Fulvic Acid and
24 Humic Acid: A DFT Exploration. *Phys. Chem. Chem. Phys.* **2011**, *13*, 18038–18046.
25
26
27
28
29
30
31
32
33
34
35
36
37
38
39
40
41
42
43
44
45
46
47
48
49
50
51
52
53
54
55
56
57
58
59
60

TOC





38
39 Figure 1. TEM micrograph of the PS-b-PAA micelles.

40 80x80mm (300 x 300 DPI)

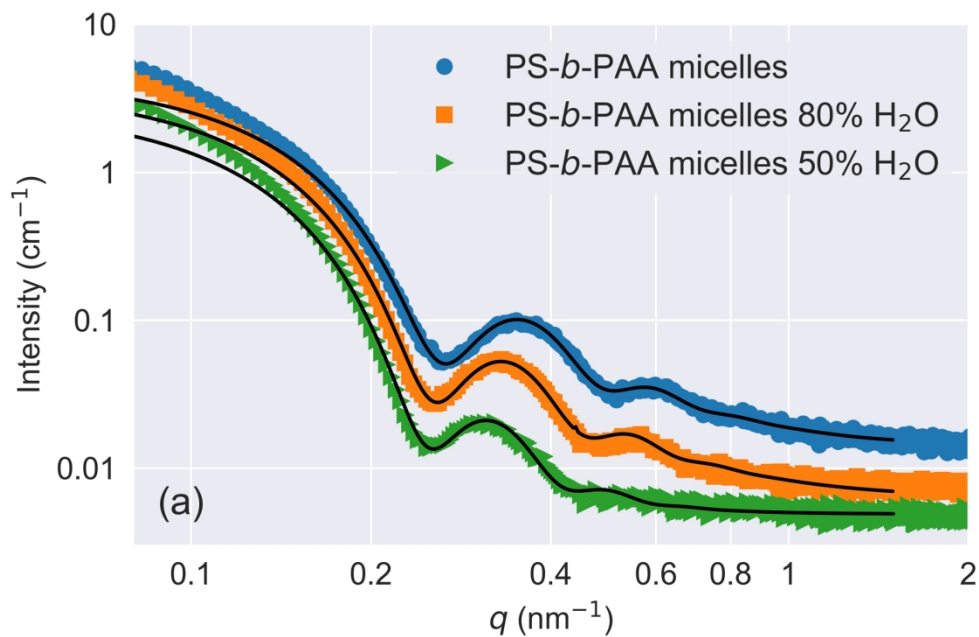


Figure 2a. SAXS curves obtained from PS-*b*-PAA micelles in H₂O and DMF/H₂O solutions (a)

84x55mm (600 x 600 DPI)

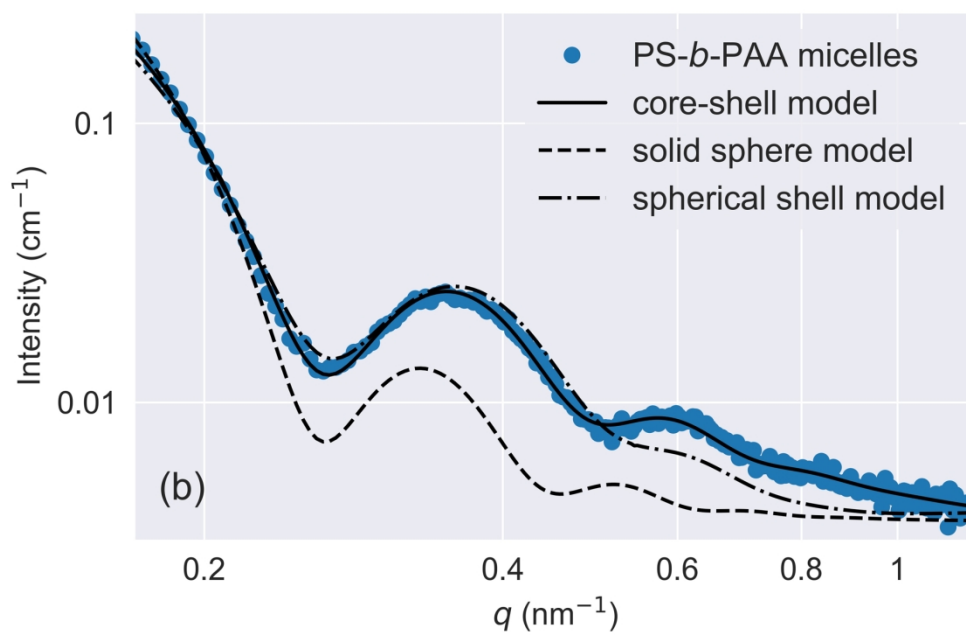


Figure 2b. Model fitting to the SAXS data of PS-*b*-PAA micelles in H₂O (b).

84x55mm (600 x 600 DPI)

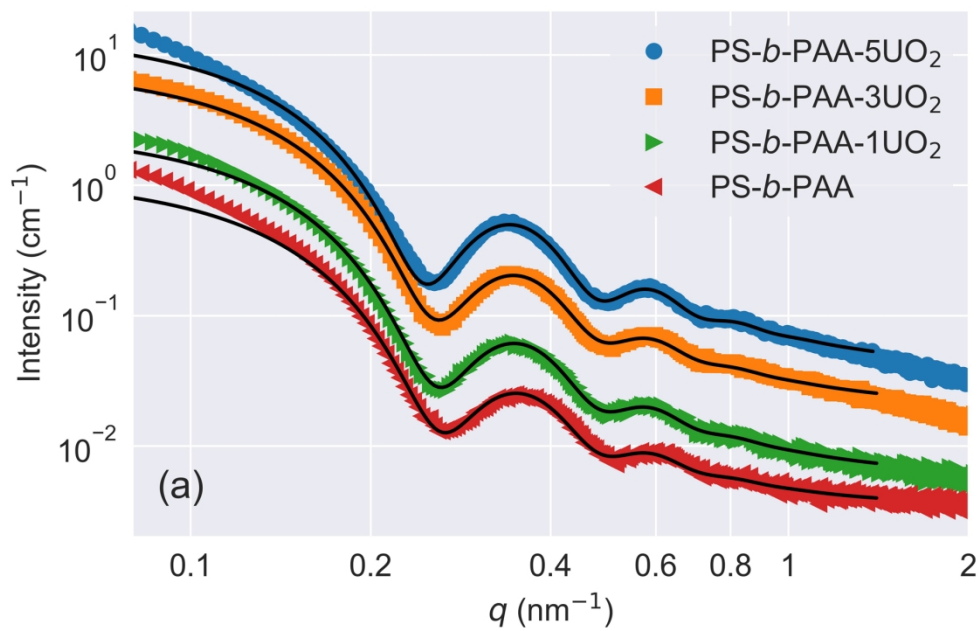


Figure 3a. SAXS curves obtained from the PS-*b*-PAA micelles and uranyl nitrate mixtures (a).

84x55mm (600 x 600 DPI)

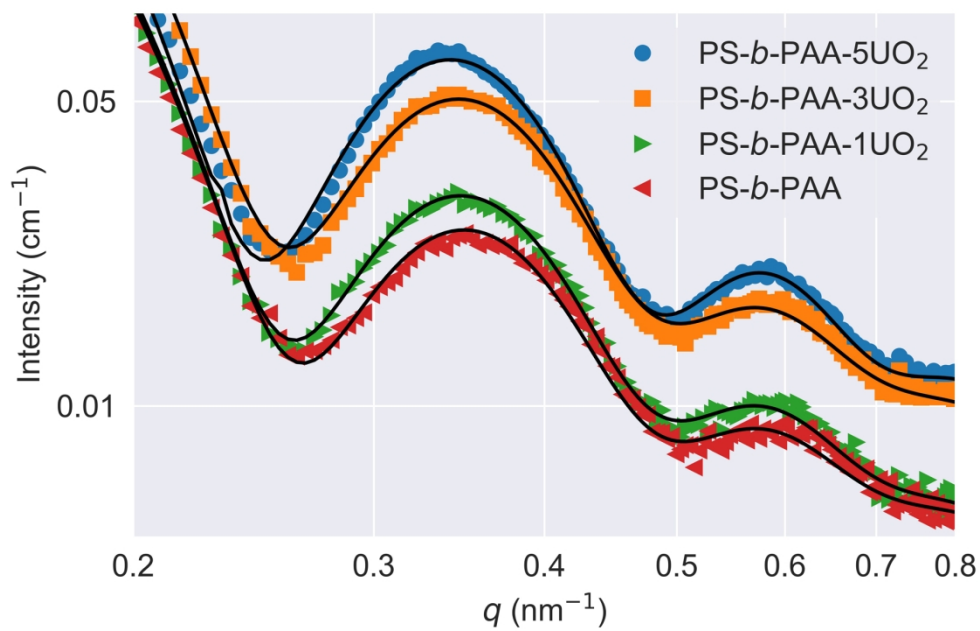


Figure 3b. A zoom-in of (a) in the medium q range (b).

83x54mm (600 x 600 DPI)

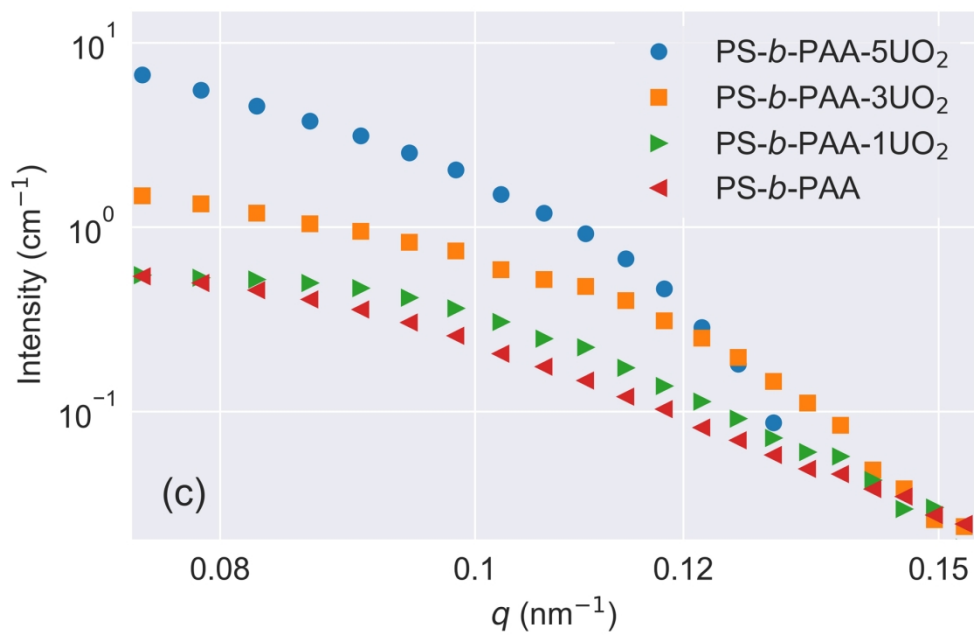


Figure 3c. Deviation between the experimental and fitted data at the low q region (c).

84x55mm (600 x 600 DPI)

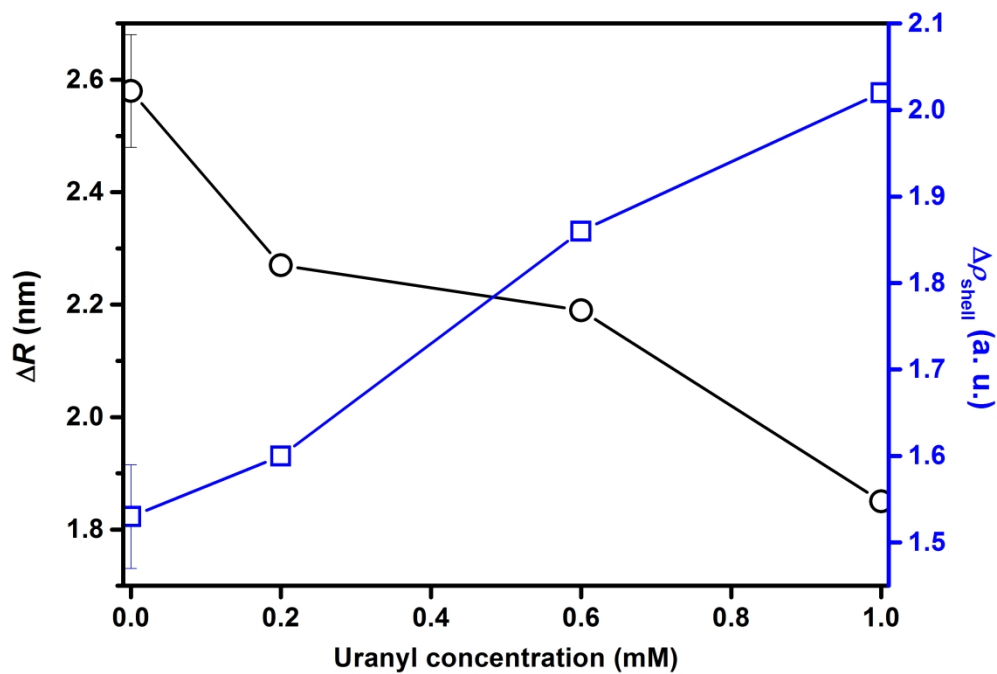


Figure 4. PAA corona thickness ΔR and contrast $\Delta\rho_{\text{shell}}$ as a function of uranyl concentration.

84x56mm (1200 x 1200 DPI)

1
2
3
4
5
6
7
8
9
10
11
12
13
14
15
16
17
18
19
20
21
22
23
24
25
26
27
28
29
30
31
32
33
34
35
36
37
38
39
40
41
42
43
44
45
46
47
48
49
50
51
52
53
54
55
56
57
58
59
60

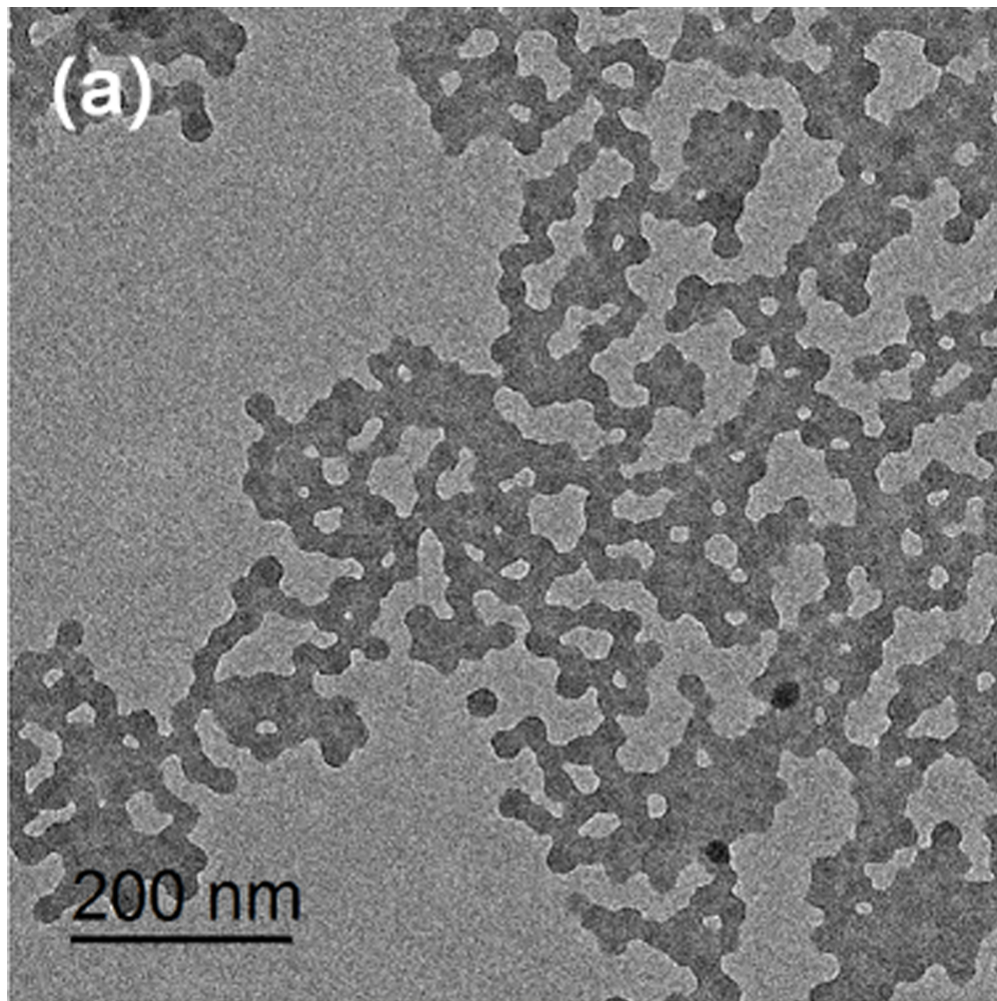
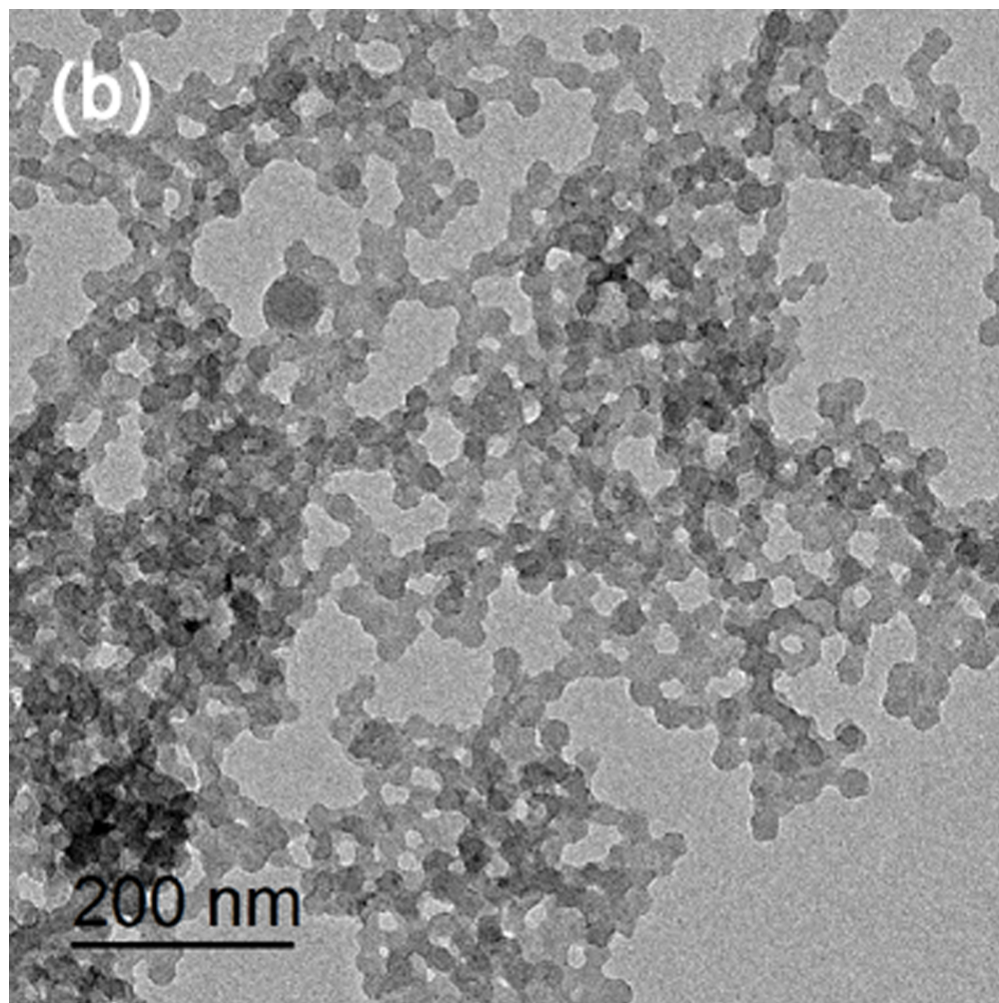


Figure 5a. TEM micrograph of the PS-b-PAA-1UO2 (a).

84x84mm (300 x 300 DPI)



38
39
40
41
42
43
44
45
46
47
48
49
50
51
52
53
54
55
56
57
58
59
60

Figure 5b. TEM micrograph of the PS-b-PAA-5UO₂ (b).

84x84mm (300 x 300 DPI)